RESEARCH ARTICLE | OCTOBER 05 2023

# Troubleshooting spectral artifacts from biplate retarders for reliable Stokes spectropolarimetry $\odot$

Ruan L. S. Lima 🗷 📵 ; Paulo T. Araújo 🗷 ; Newton M. Barbosa Neto 🗷 📵



Rev. Sci. Instrum. 94, 103102 (2023) https://doi.org/10.1063/5.0160132









# Troubleshooting spectral artifacts from biplate retarders for reliable Stokes spectropolarimetry

Cite as: Rev. Sci. Instrum. 94, 103102 (2023); doi: 10.1063/5.0160132

Submitted: 30 May 2023 · Accepted: 17 September 2023 ·

**Published Online: 5 October 2023** 









Ruan L. S. Lima, 1,a) D Paulo T. Araújo, 2,a) and Newton M. Barbosa Neto 1,a) D



### **AFFILIATIONS**

- <sup>1</sup> Institute of Natural Sciences, Federal University of Pará, Belém, PA, Brazil
- <sup>2</sup> Departament of Physics and Astronomy, University of Alabama, Box 870324, Tuscaloosa, Alabama 35487, USA
- a) Author to whom correspondence should be addressed: ruan.lima@icen.ufpa.br, paulo.t.araujo@ua.edu and barbosaneto@ufpa.br

#### **ABSTRACT**

Polarimetry is generally used to determine the polarization state of light beams in various research fields, such as biomedicine, astronomy, and materials science. In particular, the rotating quarter-wave plate polarimeter is an inexpensive and versatile option used in several singlewavelength applications to determine the four Stokes parameters. Extending this technique to broadband spectroscopic measurements is of great scientific interest since the information on light polarization is highly sensitive to anisotropic phenomena. However, the need for achromatic polarizing elements, especially quarter-wave plates, requires special attention in their modeling. In this study, we implemented a rotating retarder spectropolarimeter for broadband measurements using a commercially available quasi-achromatic biplate retarder over the visible range. Here, we present a comprehensive approach for troubleshooting this type of spectropolarimeter through the observation of artifacts stemming from the standard single-plate retarder model. Then, we derive a more suitable model for a quasi-achromatic retarder consisting of a biplate junction. This new biplate model requires knowledge of the intrinsic dispersive properties of the biplate, namely the equivalent retardance, fast axis tilt, and rotatory angle. Hence, in this study, we also show a self-consistent methodology to determine these biplate properties using the same polarimeter apparatus so that accurate Stokes parameters can be determined independently. Finally, the comparison of data generated with the standard single-plate and new biplate models shows a significant improvement in the measurement precision of the investigated polarization states, which confirms that remodeling the retarder for reliable spectropolarimetry

Published under an exclusive license by AIP Publishing. https://doi.org/10.1063/5.0160132

#### I. INTRODUCTION

Over the last decade, polarimetry has been employed to investigate a variety of systems, ranging from biology and medicine to astronomy, oceanography, and atmospheric sciences. 12,13 Characterizing light is essential in materials science, and spectropolarimetry is a new approach for obtaining additional information on anisotropic phenomena. 14,15 The conventional method for describing partially and completely polarized light relies on both the Stokes parameters of light and the Mueller matrices of polarizing elements. This formalism is written in terms of intensities of light, and linear transformations thereof. Several setups exist to evaluate the polarization state of a light beam, each with advantages and disadvantages. They all consist of some arrangement of an analyzer and a retarder. 16,17

The setup employed in this work defines the rotating retarder polarimeter, which has been chosen for its convenience. Our polarimeter relies on the modulation of transmitted light by a rotating quarter-wave plate and a fixed linear polarizer. Owing to the fixed linear polarizer, the polarization state of light immediately before detection remains unchanged.<sup>18</sup> This fixed final polarization state is essential to avoid artifacts caused by the polarizationdependent responses of diffraction gratings. 19,20 Additionally, all elements remain on the optical path, ensuring that no variation in intensity due to reflection or absorption of the elements occurs. The harmonically modulated signal is then properly adjusted according to a truncated Fourier series, whose amplitudes of specific frequencies depend linearly on the Stokes parameters. This fact makes this approach quite convenient, as the polarization information can be separated from spurious regular oscillations in intensity, such as source instability.<sup>21</sup> This method has been used in various single-wavelength applications. For instance, Alliprandini-Filho *et al.*<sup>22,28</sup> and Therézio *et al.*<sup>27,28</sup> have published several works applying it to investigate the polarized emission of organic molecular systems in solution and as thin films.

More recently, attempts have been made to automate this procedure using compact and portable polarimeters, but only at specific wavelengths.<sup>29,30</sup> Automated systems have already been suggested and successfully applied to a more robust technique called Mueller Matrix Ellipsometry (MME),<sup>31-37</sup> where all elements of a sample's related matrix can be determined. Currently, MME is widely used for determining the thickness and optical properties of thin films and crystals based on spectropolarimetric analysis of the reflected beam 17,38-40 over a broad wavelength range. This technique assumes a specific reflection geometry, where the light source and detector are equally inclined from the surface. In addition, the MME requires two pairs of synchronously rotating achromatic wave plates and linear polarizers: one for polarization generation before reflection and the other for polarization analysis after reflection. A recent variation of the rotating retarder polarimeter was published by Hawley et al.41 They used a Fresnel cone to statically produce the same effect as a rotating retarder. In their system, rotation over time is equivalent to different positions of a structured light beam, which enables a one-shot broadband polarimeter. The optical path geometry and the elements involved, such as the Fresnel cone, could make this variation inconvenient for many applications.

Several studies in the literature examined defects in polarizing elements for polarimetric applications. For instance, in the context of MME, Hauge<sup>34</sup> presented various methods for determining Mueller matrices with imperfect elements using calibration methods. However, he did not show experimental results and did not consider spectral artifacts caused by such imperfections. Furthermore, the effect of the misalignment of the fast axis angular position on the measurement of Stokes parameters has been investigated for single-wavelength rotating retarder polarimetry, and methods to circumvent this issue have been presented.<sup>42</sup> Similarly, other studies have investigated the influence of misalignment of the polarizer and deviations in the retardance of a waveplate on the measured Stokes parameters, but they do not provide general methods for the characterization of the retarder. <sup>43,44</sup> An automated rotating retarder Stokes polarimetry was also developed, and the results showed that neglecting the actual value of the retarder's retardance yields inaccurate Stokes measurements. In addition, the influence of mechanical disturbances on the results was evaluated.4

Since the present work requires achromatic elements for spectral measurements, a single-wavelength approach is insufficient. Achromatic elements have been widely developed in recent decades, particularly achromatic retarders, which are crucial for spectropolarimetry. In this framework, it is crucial to investigate how achromatic retarders lead to polarizing artifacts owing to manufacturing errors. Several studies have explained that achromatic quarter-wave retarders are usually manufactured as a multiplate assembly of birefringent crystals with orthogonally aligned optical axes. 46,47 However, perfect alignment is impractical, and the angular offset between crystals results in an imperfect achromatic retarder. Owing to the dispersive properties of the materials used, the retardance of a quarter of a wave cannot be guaranteed over a broad spectral range, and

the biplate's fast axis azimuth becomes wavelength-dependent, producing a spurious effect in the transmitted light. Based on Jones' optical equivalence theorem,  $^{48}$  any multiplate retarder is optically equivalent to a rotated retarder followed by a pure rotator, which considerably simplifies the mathematical description. In our case, the achromatic quarter-wave retarder was a biplate composed of crystalline quartz and magnesium fluoride  $(\mathit{MgF}_2)$  with individual fast axes at nearly orthogonal relative positions. Thus, the conditions for modeling it as an equivalent system are sufficient. As discussed below, we observed strong dispersive artifacts, indicating that the intrinsic properties of the biplate equivalent system, such as retardance and fast axis position, cannot be taken ideally like in the standard model, as usually done.  $^{49-56}$ 

A similar rotating retarder approach has been used to probe the state of emission, Raman scattering, and transmission of organic materials, such as liquid crystals and chiral copolymers. 49-51,54-56 In these works, the system was reported to contain specific achromatic elements to enable measurements of spectral distributions of Stokes parameters and relate them to anisotropic properties such as the degree of polarization, linear anisotropy, and asymmetry factor.<sup>57</sup> One important step for the proper application of this technique is its calibration, which they often omit owing to their focus on applications. Therefore, to circumvent these problems, we developed a more reliable biplate-retarder model for measurements of Stokes parameter dispersions, where the biplate assembly and optical equivalence are considered. Here, we provide the necessary steps to properly set up the apparatus, evaluate the manifestation of artifacts related to the dispersive properties of the retarder, and derive a more suitable model for the rotating biplate-retarder polarimeter. We then present experimental methods for measuring the intrinsic dispersive equivalent properties of the biplate, which arise from the new model, using the same polarimeter apparatus, thereby establishing a self-contained setup for broadband applications. Finally, a direct comparison of the single- and biplate model results is discussed.

# II. FUNDAMENTALS: STOKES PARAMETERS, ELLIPSE OF POLARIZATION. DEGREE OF POLARIZATION

A description of an arbitrary partially polarized light beam and its transformation by optical elements can be achieved through the Stokes–Mueller formalism. In this formalism, the modification of the intensity and polarization properties of a light beam owing to its propagation in an optical element is represented by a linear transformation of a vector by a matrix. This formalism relies on the time-averaged behavior of the ellipse of polarization [see Fig. 1(a)]. The four Stokes parameters contain all the averaged electric field parameters, that is, the amplitudes of the x- and y-components ( $E_{0x}$  and  $E_{0y}$ ) and the phase difference between them ( $\delta = \delta_x - \delta_y$ ). In other words, the time-averaged dynamical pattern of the electric field in a transverse plane to propagation (ellipse of polarization) is fully contained within the Stokes parameters of light. Such parameters are defined as  $^{18,58-60}$ 

$$\vec{\mathbb{S}} = \begin{bmatrix} \mathbb{S}_0 \\ \mathbb{S}_1 \\ \mathbb{S}_2 \\ \mathbb{S}_3 \end{bmatrix} = \begin{bmatrix} E_{0x}^2 + E_{0y}^2 \\ E_{0x}^2 - E_{0y}^2 \\ 2E_{0x}E_{0y}\cos\delta \\ 2E_{0x}E_{0y}\sin\delta \end{bmatrix}$$
(1)

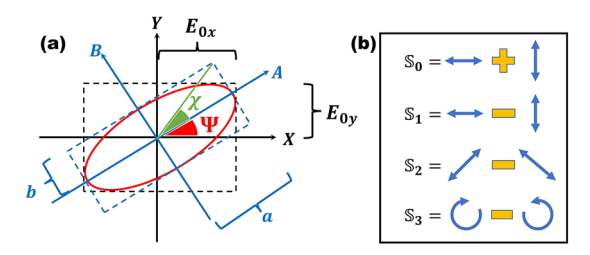


**FIG. 1.** (a) Scheme of ellipse of polarization and its geometric properties: elliptical inclination  $(\Psi)$  and ellipticity  $(\chi)$ . The Cartesian amplitudes of the electric field are represented in the laboratory coordinate system  $(E_{0x}$  and  $E_{0y}$  in the X–Y black axes), for which the ellipse is rotated by  $\Psi$ , and in the ellipse reference system (a and b in the A-B blue coordinates), for which the ellipse is unrotated, but exhibits an ellipticity of  $\chi$ , associated with the relative size of semi-minor axis b to semi-major axis a. (b) Scheme of differential definition of the Stokes parameters of light  $(\mathbb{S}_0,\mathbb{S}_1,\mathbb{S}_2,\mathbb{S}_3)$ , where each parameter represents the difference between two intensities of orthogonal pure-polarization states. Such states define a polarization-basis set, upon which any other arbitrary polarization state can be described.

such that the "completeness" condition is satisfied as follows:

$$S_0^2 \ge S_1^2 + S_2^2 + S_3^2. \tag{2}$$

In Eq. (2), the equal sign only holds for completely polarized light, which satisfies the condition that the time average of the phase difference of the components is a constant. Figure 1(b) shows a schematic of a qualitative alternative definition for the Stokes parameters as the difference of intensities, which better conveys their observable characteristics.  $^{18,60,61}$  As shown, the  $\mathbb{S}_0$  parameter represents the total intensity of light measured, while  $S_1$  represents the unbalance between the intensities of horizontal and vertical linear components,  $S_2$  represents the unbalance between the intensities of diagonal and anti-diagonal linear components, and S3 represents the unbalance between the intensities of clockwise (right-handed) and counterclockwise (left-handed) circular components. It is worth noting that  $(S_1, S_2, S_3)$  are zero for unpolarized light, as light in this polarization state statistically oscillates in all directions. We will refer to the term  $\mathbb{S}_0^p = \sqrt{\mathbb{S}_1^2 + \mathbb{S}_2^2 + \mathbb{S}_3^2}$  the polarized intensity since this parameter is limited to the total intensity of light,  $S_0$ , according to Eq. (2), and is zero for unpolarized light. In other words, the sum of the polarized portions of light is always at most equal to the total intensity of light.

Upon that, we can define the *Stokes-fractions*  $(s_1, s_2, s_3)$ , or normalized Stokes parameters relative to the total intensity, which are given by

$$s_k = \mathbb{S}_k / \mathbb{S}_0, \quad k = 1, 2, 3.$$
 (3)

Furthermore, we can define a parameter to describe the fraction of polarized light within an arbitrary partially polarized light beam, the *degree of polarization*, as

$$P = \sqrt{\mathbb{S}_1^2 + \mathbb{S}_2^2 + \mathbb{S}_3^2} / \mathbb{S}_0 = \sqrt{s_1^2 + s_2^2 + s_3^2}.$$
 (4)

These definitions are particularly relevant for handling partially polarized light, where 0 < P < 1. In this situation, the unpolarized and completely polarized portions of light may be distinguished,

since the unpolarized portion has  $s_{(1,2,3)}=0$ , and only the polarized portion contributes to the polarization characteristic of that beam, with  $s_{(1,2,3)}\neq 0$ . In particular,  $s_1=+1(-1)$  represents horizontally (vertically) polarized light,  $s_2=+1(-1)$  represents  $+45^\circ$  ( $-45^\circ$ ) linearly polarized light, and  $s_3=+1(-1)$  represents clockwise (counterclockwise) circularly polarized light. Hence, these states with unitary Stokes fractions,  $s_{(1,2,3)}=\pm 1$ , form a polarization-basis set, upon which every other intermediate state have partial contributions of each of those fundamental states.

Every polarization state of a light beam can be described by a unique ellipse with an ellipticity angle  $(\chi)$  and an inclination angle  $(\Psi)$ , as represented in Fig. 1(a). These angles can be related to the wave's amplitudes and their relative phase difference, and consequently to the Stokes parameters of light via Eq. (1), as given by the following equations:<sup>18</sup>

$$\tan(2\Psi) = \mathbb{S}_2/\mathbb{S}_1,\tag{5a}$$

$$\tan(2\chi) = S_3/\sqrt{S_1^2 + S_2^2}.$$
 (5b)

These angles are defined relative to the semi-major and semi-minor axes, a and b, respectively, as shown in Fig. 1(a), and they range from  $-45^{\circ}$  to  $45^{\circ}$  for  $\chi$  and  $0^{\circ}$  to  $180^{\circ}$  for  $\Psi$ . Hence, we can see that the Stokes parameters fully describe the polarization state of any beam. Therefore, what we call *Stokes polarimetry* is a method to determine the Stokes parameters of light, from which the fraction of polarized light may be distinguished from the unpolarized portion and be fully described in terms of elliptical angular parameters, given by Eqs. (5a) and (5b).

# III. THE STANDARD MODEL: IDEAL ROTATING RETARDER POLARIMETER

Among the methods to determine the Stokes parameters of light, 16,62 the rotating retarder polarimetry (RRP) method consists of the modulation of transmitted light over different angular positions of a quarter-wave retarder followed by a fixed horizontal polarizer. To describe this method mathematically, the Mueller matrix formalism is used (see Sec. S1 of supplementary material]. It consists in taking any polarizing optical element as a 4 × 4 matrix capable of linearly transforming a Stokes vector, that is, a pseudo-vector containing all four Stokes parameters. To derive the equation that describes how the modulation of the transmitted intensity of light depends on the Stokes parameters of the incoming beam, we utilize the accumulative property of transformations that results from the elements used in the setup, which include a rotating quarter-wave retarder and an analyzer. 18 This calculation yields the modulation of the transmitted intensity described in terms of either the Stokes fractions ( $s_k = \mathbb{S}_k/\mathbb{S}_0$ , k = 1, 2, 3),

$$I(\theta) = \frac{\mathbb{S}_0}{2} \left[ \left( 1 + \frac{s_1}{2} \right) + \frac{s_1}{2} \cos\left(4\theta\right) + \frac{s_2}{2} \sin\left(4\theta\right) + s_3 \sin\left(2\theta\right) \right]$$
 (6)

or, more generally, in terms of amplitude parameters  $(A_i, i = 0, 1, 2, 3)$ , as

$$I(\theta) = \frac{1}{2} [A_0 + A_1 \cos(4\theta) + A_2 \sin(4\theta) + A_3 \sin(2\theta)]$$
 (7)

such that,

$$A_0 = \mathbb{S}_0 + \mathbb{S}_1/2,$$
 (8a)

$$A_1 = \mathbb{S}_1/2,\tag{8b}$$

$$A_2 = \mathbb{S}_2/2,\tag{8c}$$

$$A_3 = \mathbb{S}_3, \tag{8d}$$

which are only valid under the assumptions that the retarder utilized has a retardance of  $2\pi/4$ , and that its fast axis position is well known as at  $\theta$  degrees counterclockwise from the vertical position.

According to Eq. (7), the intensity modulation follows a harmonic pattern represented by a truncated Fourier series. The amplitudes of specific frequencies (0, 2, and 4) in this series are linearly dependent on the Stokes parameters of the analyzed beam. Consequently, the Stokes parameters can be determined from the manipulation of particular amplitudes obtained from Fourier analysis of the modulated transmitted signal. To determine the amplitude parameters, we can use a discrete Fourier transform of the experimental data at each wavelength. The data is discrete because the waveplate is rotated in finite steps ( $\Delta\theta$ ); usually 36 steps of 10°, but 18 steps of 20°, 12 steps of 30°, or 9 steps of 40° are also possible. Thus, the amplitudes can be calculated using the following equation, as described in Ref. 18:

$$A_0 = \frac{2}{N} \sum_{n=1}^{N} I(n\Delta\theta), \tag{9a}$$

$$A_1 = \frac{4}{N} \sum_{n=1}^{N} I(n\Delta\theta) \cos(4n\Delta\theta), \tag{9b}$$

$$A_2 = \frac{4}{N} \sum_{n=1}^{N} I(n\Delta\theta) \sin(4n\Delta\theta), \tag{9c}$$

$$A_3 = \frac{4}{N} \sum_{n=1}^{N} I(n\Delta\theta) \sin(2n\Delta\theta), \tag{9d}$$

where  $I(n\Delta\theta)$  is the transmitted intensity for the retarder's fast axis at the n-th step of  $\Delta\theta$ , and the summation runs over all angular positions until a complete round.

### IV. THE EXPERIMENTAL SETUP

The Stokes parameters are obtained through the Fourier analysis of the transmitted signal. In this method, the light beam under analysis, regardless of its origin, is properly collimated and directed through a rotating quarter-wave retarder, followed by a fixed horizontal polarizer (analyzer). As mentioned above, the RRP involves acquiring a transmission spectrum at each angular position of a rotating quarter-wave retarder (QWR). As we intend to take spectral measurements, all elements have to be achromatic. The light is detected by a spectrometer, which allows signal acquisition at several wavelengths.

In this study, we implemented a spectral version of the RRP by aligning the appropriate elements, as shown in Fig. 2, so that any incoming light beam may be polarimetrically resolved over a broadband spectrum. The quarter-wave retarder used is a double-crystal junction of crystalline quartz and magnesium fluoride  $(MgF_2)$ , purchased from Thorlabs as achromatic in the 400-800 nm range. The retarder is mounted in a rotating stage with angular precision of 2°. For our experiments, the retarder is rotated around the light transmission direction from  $0^{\circ}$  to  $360^{\circ}$  in steps of  $10^{\circ}$ , which accumulates 37 transmission spectra. The analyzer used is a 10 mm mounted Glan-Laser calcite polarizer, also purchased from Thorlabs, which was placed in a platform with three angular adjustments, and then aligned to horizontal with a bubble level. As this element is uncoated, its transmission is suitably achromatic from the ultraviolet-visible (UV-Vis) to near-infrared range. Moreover, we used a portable USB CCD spectrometer from Ocean Optics as the detector, with optical sensibility covering the 200-890 nm range. This allowed us to acquire a whole spectrum at once and evaluate transmission signal in real time.

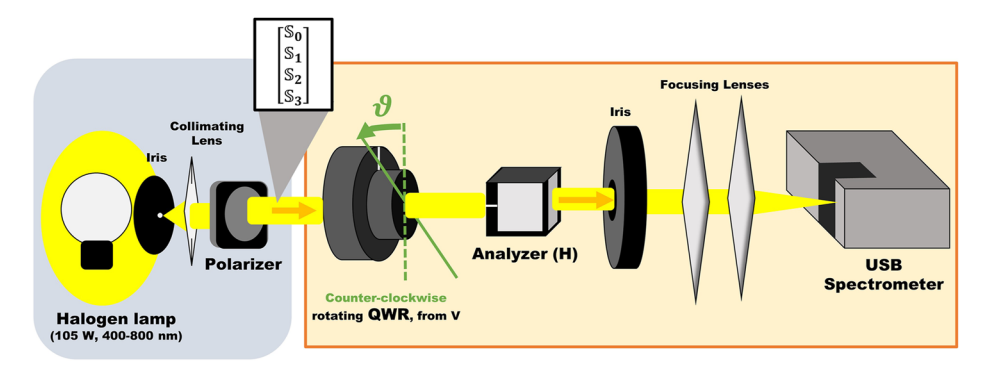


FIG. 2. General scheme of experimental apparatus utilized in this work. The polarization generator stage is represented inside the blue box and contains, respectively, a halogen incandescent light bulb (105 W, with emission across 400–800 nm), an iris and a lens for collimation, and a polarizer (linear or circular) to set the incident polarization, represented by the Stokes parameters in the white box inset, toward the polarimeter. The elements for the Rotating Retarder Polarimetry (RRP) are displayed within the orange box. The representation of labeled elements of RRP from the left to the right: the rotating quarter-wave retarder (rotated by  $\vartheta$  counterclockwise relative to the detector, with fast axis starting at mark  $\vartheta=0^\circ$  in the vertical direction), the analyzer (a Glan-laser calcite polarizer aligned with transmission axis in the horizontal direction) and the spectrometer (Ocean Optics 2000). In the retarder, (V) stands for the retarder's fast axis initial direction at vertical and (H), in the analyzer, stands for transmission axis at horizontal.

A broadband light source with a controllable polarization state has been implemented, as represented in Fig. 2. The light source used was a 105 W halogen incandescent lamp, whose emission spectrum covered the visible range of 400-800 nm. The beam was properly collimated for calibration measurements and the polarization state of this broadband beam was controlled with two different polarizers. A calcite polarizer was used as a linear polarizer filter to create 0° (horizontally), 30°, 45°, 60°, and 90° (vertically) linearly polarized light to be analyzed with the assembled system. The angular positioning of this linear polarizer was made by assembling the crystal in a rotation mount with precision of 2° and adjusting the angles manually. The transmission axis was approximately set at the mount's  $0^{\circ}$  mark in the vertical direction by fixing the mount, and rotating the crystal until transmitted light spectrum through polarizers reached a minimum when they became crossed (polarizer at vertical and analyzer at horizontal). See Sec. S2.1 of the supplementary material for further information about the polarization capacity of such polarizer.

Additionally, a circular polarizer filter was also used as a non-linear state reference, which produced a polarization state labeled as elliptically polarized light (EPL), since such filters are not usually manufactured to be achromatic. This element is often used in photography to filter glare and functions as a combination of a linear polarizer inclined 45° to a birefringent film's fast axis to produce circular polarization at some wavelength. Since this birefringent film is not achromatic, a perfectly broadband circularly polarized light cannot be assured. Nonetheless, it served as a suitable calibration for proving that we can measure arbitrary elliptical polarization state as well.

It is noteworthy that detection done by the USB2000 Ocean Optics spectrometer allows us to acquire spectra with three basic adjustments: integration time, scans to average, and boxcar width. Those detection settings, respectively, control the amount of time for a photon accumulation, the spectral smoothing over time (time-averaging), and the spectral smoothing over wavelength (wavelength-averaging). Hence, all experimental data presented in this work were acquired with optimized detection settings, where integration time was set to avoid saturation in detection during measurements (often within 3-100 ms), the number of scans to average was set so that the overall spectral intensity with retarder at a particular position would not oscillate much (within 15-20 scans), and the boxcar width was set to smooth spectrum below the point it became distorted (within 15-20 pixels). Therefore, the sources of oscillations in detected intensities unrelated to the angular position of the retarder, which would lead to significant error bars in our measurements, were all hindered by controlling detection settings (see Sec. S2.2 of the supplementary material).

With the system assembled (see Fig. 2), we measured the transmission spectra in different angular positions of the retarder to obtain the Stokes parameters. Starting with its fast axis in the vertical position (V), at 0°, and it was rotated counterclockwise (relative to the detector's viewpoint). The intensity at each wavelength is modulated harmonically with the retarder's rotation, as described by a truncated Fourier series in Eq. (7). The Stokes parameters for each wavelength are then obtained by linearly manipulating the amplitude of specific frequencies, which is given by Eq. (8) in the simplest case where all elements are ideal. To perform the data processing, we developed a program in MATLAB that runs a loop over wavelength, so the spectra of Stokes parameters could be obtained.

# V. EXPERIMENTAL INDICATORS OF INADEQUATE MODEL FOR SPECTRAL MEASUREMENTS

# A. Transmission modulation of horizontally polarized light (HPL) over $\theta$ at some $\lambda$

Based on the standard model, which assumes a waveplate causing a maximum phase shift of  $90^{\circ}$  and a known fast axis position at a counterclockwise angle of  $\theta$  from the vertical direction, the transmitted intensity is modulated as the retarder rotates, as described by Eqs. (7) and (8). When applied to the situation where the incoming light is horizontally polarized, such that the total-Stokes-fractions are  $[s_1, s_2, s_3) = (+1, 0, 0)$ , Eq. (7)] yields Eq. (10),

$$I_H(\theta) = \frac{\mathbb{S}_0}{4} [3 + \cos(4\theta)]. \tag{10}$$

Observe that since the intensity modulation over  $\theta$  for HPL is harmonic, it has a maximum and a minimum. The theoretical ratio between minimum and maximum values is thereby expected to be

$$I_H^{\min}/I_H^{\max} = 1/2.$$
 (11)

However, as depicted in Fig. 3(a), the experimental transmission signal for HPL at 532 nm, represented by the green diamond symbols, reveals that the minimum intensity of the modulation normalized by the maximum intensity falls below 0.5. This requires that to fit the experimental data, the theoretical model given by Eq. (6) when all parameters are free to vary (as the red solid curve) had to yield  $(s_1, s_2, s_3) = (1.40, -0.07, -0.01)$ , that is, P > 1. This result would represent an unrealistic scenario of more polarized light than what is actually detected, which is physically implausible. Conversely, by fixing the fit parameters to be  $(s_1, s_2, s_3) = (+1, 0, 0)$  in Eq. (6), the theoretical curve cannot appropriately adjust the experimental data, as shown as the blue solid curve.

Thus, this observation indicates that the existing single-plate model lacks the necessary information to accurately fit the experimental data. The issue of P exceeding unity appears to stem from miscalculation of the Stokes parameters, indicating that the relations between the amplitudes of the Fourier series and the values of the Stokes parameters, described in Eq. (8), require proper revision. It is important to highlight that the error bars associated with the experimental data are omitted since the detection settings (integration time, scans to average, and boxcar width) are optimized to hinder sources of error in intensity, which yield below 1% standard deviation. See Sec. S2.2 of the supplementary material for more details.

# B. Transmission modulation of vertical polarized light (VPL) over $\lambda$ at some $\theta$

In Fig. 3(b), we analyze the transmitted spectra through crossed polarizers (polarizer at V and analyzer at H) and the biplate in between with fast axis at specific angular positions  $\pm 2^{\circ}$  from the vertical mark. It is worth noting that this setup resembles a regular experimental setting for the measurement of Stokes parameters, as described in Sec. III. The hachured black curve in Fig. 3(b) represents the transmitted spectrum of crossed polarizers alone, with the retarder removed from the optical path, revealing only a small residual transmitted light at each wavelength attributed to the efficiencies of the polarizers, which can be enhanced when

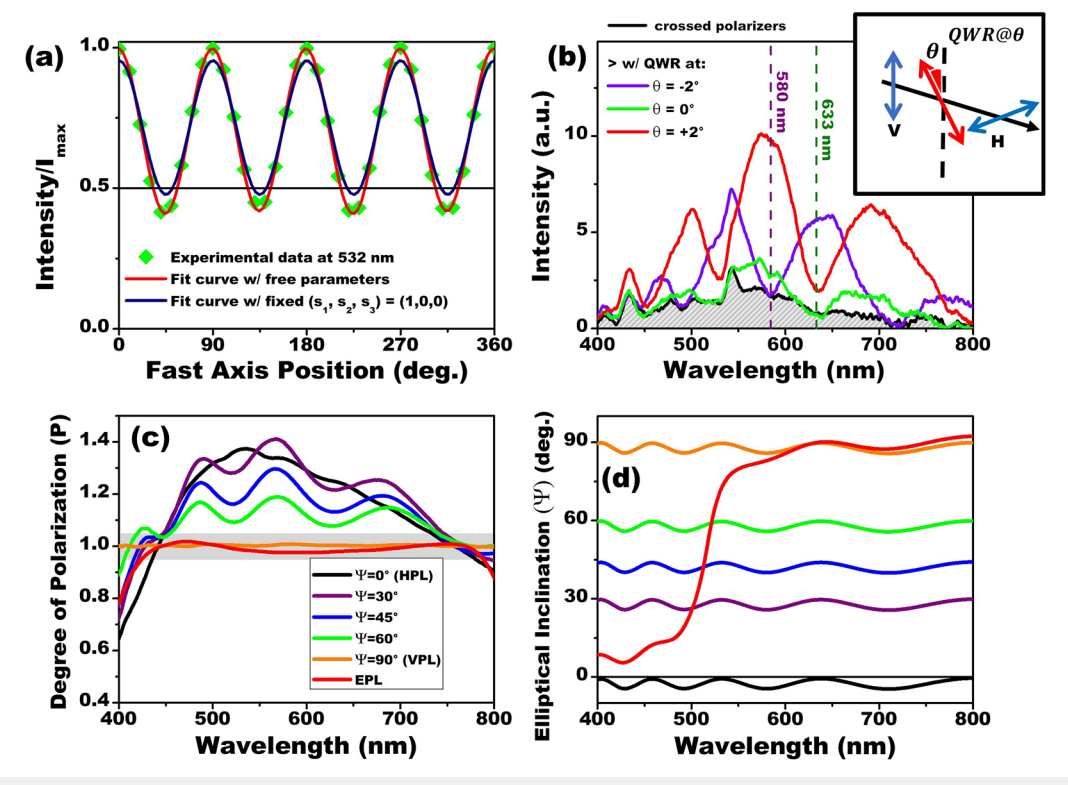


**FIG. 3.** Experimental indicators of inadequate model for spectral measurements. (a) and (b) show direct measurements of light intensity, whereas (c) and (d) display calculated results that consider the single plate model. (a) Transmission intensity modulation of horizontally polarized light at 532 nm as function of retarder's fast axis position, normalized by maximum intensity, in green diamond symbols. The solid red line indicates a theoretical fit curve with single-plate model, given in Eq. (6), which yield  $(\mathbf{s}_1, \mathbf{s}_2, \mathbf{s}_3) = (1.40, -0.07, -0.01)$  for fit convergence. The solid dark blue curve represents the theoretical fit curve for which the condition  $(\mathbf{s}_1, \mathbf{s}_2, \mathbf{s}_3) = (+1, 0, 0)$  are fixed, while  $\mathbb{S}_0$  is free to vary, as in Eq. (10). (b) Spectra of transmitted light through crossed polarizers, as the hachured black curve, and the retarder in between with fast axis at  $-2^\circ$  (violet solid line), 0° (green solid line), and  $+2^\circ$  (red solid line) from vertical position. Vertical dashed dark green line marks 633 nm position, whereas dashed purple line marks 580 nm. The inset shows a scheme of the configuration of elements for such measurements. (c) Degree of polarization spectra  $[P(\lambda)]$  calculated with the single-plate model for various incoming polarization states: from  $\Psi = 0^\circ$  (HPL) to  $\Psi = 90^\circ$  (VPL), and elliptically polarized light (EPL). A gray shadowed area highlights the range of values within  $\pm 5^\circ$  accuracy from unity. (d) Elliptical inclination angle spectra  $[\Psi(\lambda)]$  calculated with the single plate model for the same various incoming polarization states

the integration time of the spectrometer is increased to enable the following analysis. The blue, green, and red curves represent the transmitted spectra with the retarder inserted between the crossed polarizers, with fast axis at  $-2^{\circ}$ ,  $0^{\circ}$ , and  $+2^{\circ}$  from the vertical direction in the laboratory, respectively. In this setup, it is expected that when the fast axis of the retarder is aligned parallel to the plane of polarization of the incoming light (that is, vertical), and the fast axis direction is the same for all wavelengths analyzed, the transmitted spectrum with the retarder should remain unchanged. This is because the beam would be affected only by the lowest refractive index for all wavelengths, with no change in the polarization.

However, the results depicted in Fig. 3(b) reveal that the transmission spectra with and without the retarder at 0° (vertical) are slightly different, and small angular deviations of retarder from zero position intensify the undulated pattern. Additionally, the vertical red dashed line in the figure represents the position of 633 nm, which is the wavelength conventionally used by the manufacturer for calibrating the fast axis position of the retarder and marking

it on the crystal's mount. It is noteworthy that the intensity at 633 nm remains the same with and without the retarder in the optical path at an angular position, indicating its fast axis position. Although, we notice that the angular position at which occurs an intensity-matching appears to depend on the wavelength being evaluated, suggesting that the fast axis position for each wavelength is slightly tilted from the mark made on the mount based on the signal at 633 nm.

In Fig. 3(b), the transmitted spectrum with retarder at  $+2^{\circ}$  exhibits a local minimum at 633 nm near the crossed intensity, whereas a local maximum is observed at  $-2^{\circ}$ , and a match with the crossed (polarizer at V and analyzer at H) intensity is seen at  $0^{\circ}$ , indicating that the manufacturer's mark agrees with expected position for 633 nm but fails for other wavelengths. However, for other wavelengths, for example, at around 580 nm (purple vertical dashed line), we observe a match with crossed intensity from the transmission spectrum with retarder at  $-2^{\circ}$ , while the spectrum for  $0^{\circ}$  does not match. This suggests that the fast axis position for this biplate, over this range of wavelengths, exhibits dispersion and deviates from

the assumption that the  $\theta$  is the same for all wavelengths, as assumed in Eq. (7).

### C. Flawed degree of polarization dispersion

In Fig. 3(c), we present the degree of polarization (P) for various incoming polarization states, which are calculated from the Stokes parameters of light estimated from the amplitudes of the truncated Fourier series, assuming the model given by Eqs. (7) and (8). The initial polarization states were selected to compare the change in  $(S_1, S_2, S_3)$  in the experimental results, that is, to compare the change in  $\Psi$  and  $\chi$  in the behavior of  $P(\lambda)$ . The angles presented in the label represent the elliptical inclination, relative to the laboratory's horizontal and counterclockwise directions to the detector, of linearly polarized light, as depicted in Fig. 1(a); all generated with a rotating calcite polarizer. The elliptically polarized light (EPL) beam is generated with a non-achromatic circular polarizing filter and is used here to represent an overall non-linear elliptical state. The created polarization state is counterclockwise elliptically polarized and circularly polarized at around 510 nm. Two observations from Fig. 3(c) indicate flawed calculations. First, for all states except VPL ( $\Psi = 90^{\circ}$ ) and EPL ( $\Psi$  is dispersive), the calculated degree of polarization is above unity, which is already known to be a physical absurdity. Second, for all off-axis states (30°, 45°, and 60°), apart from being mostly above one, the dispersion of degree of polarization is strongly modulated over wavelengths, which cannot be attributed to the calcite polarizer. Both of these observed flaws indicate that the model used is inadequate in determining the spectral distribution of Stokes parameters accurately with this apparatus.

### D. Flawed elliptical inclination dispersion

Finally, in this section, we present the dispersion of elliptical inclination (Ψ) in Fig. 3(d), which has been calculated using the same data employed to estimate the degree of polarization. The results displayed in Fig. 3(d) reveal a consistent modulation over the spectrum for all generated states, suggesting that the currently utilized single plate model does not explain the experiments. Notably, all the maxima and minima of the modulation align perfectly for all states, which suggests that these curves are influenced by an additional term not accounted for in the currently employed model. Additionally, it is noteworthy that for wavelengths ranging from 450 to 500 nm, where in Fig. 3(c) we see the degree of polarization of the EPL curve slightly above one, the elliptical inclination, depicted in Fig. 3(d) (red line), tends to be more horizontal, hovering near  $0^{\circ}$ . This behavior aligns well with the HPL trend, as evident from Fig. 3(c), indicating a correlation between the above-unit trend in degree of polarization shown in Fig. 3(c) and the elliptical inclination in Fig. 3(d).

While the dispersions of Stokes parameters, which were used to calculate the degree of polarization and the elliptical inclination, have been omitted for the sake of simplicity (see Sec. S3 in the supplementary material for more data), it is important to note that the observed spectral artifacts, such as modulations and above-unity issues, are also evident in those parameters. In fact, a more comprehensive analysis would reveal similar trends across all parameters. In light of this, we will now proceed to discuss a more complete model for a quasi-achromatic biplate retarder, taking into consideration additional information about the retarder to address these observed spectral artifacts.

# VI. BIPLATE MODEL: STOKES POLARIMETER WITH QUASI-ACHROMATIC BIPLATE RETARDERS

A biplate model accurately describes a rotating-biplate-retarder polarimeter, in which the retarder is designed to be quasiachromatic within a specific range. This is achieved by assembling two birefringent crystals; in our case, quartz and MgF2. Previous studies<sup>63–68</sup> have shown that a misaligned biplate assembly, designed to function as a quasi-achromatic waveplate, is equivalent to a single rotated retarder followed by a rotator, according to Jones's equivalence theorem.<sup>48</sup> Therefore, we must adapt, while still using the Mueller matrix formalism, the standard model for a better description of real optical elements. Here, the biplate assembly is equivalent to a single retarder with retardance  $\phi = \phi(\lambda)$ , where the fast axis rotated counterclockwise from the *vertical* position by  $\theta = \theta(\lambda)$ , followed by a pure rotator that rotates the plane of polarization counterclockwise by  $\rho = \rho(\lambda)$ , as depicted in Fig. 4(a). As a result, the RRP system can be represented by a Mueller matrix, which is given by

$$M_{S} = M_{P}^{H} \{ M_{R}(2\rho) [M_{R}(-2\theta) M_{W}^{V}(\phi) M_{R}(2\theta)] \},$$
 (12)

where  $M_W^V(\phi,2\theta)=M_R(-2\theta)M_W^V(\phi)M_R(2\theta)$  represents the Mueller matrix of an arbitrary retarder with retardance  $\phi$ , rotated by  $\theta$  from vertical.  $M_R(2\rho)$  is the matrix for the equivalent pure rotator, and  $M_P^H$  represents the matrix of an ideal linear horizontal polarizer, that is, the analyzer with the transmission axis in the horizontal direction. The explicit form of each matrix utilized here can be found in Sec. S1 of the supplementary material. Since we can only detect the total intensity of the beam emerging from the polarizing elements, the Stokes vector of the detected beam,  $\vec{\mathbb{S}}_{out}$ , carries the total transformation experienced by the incoming beam, which contains the polarization state that shall be measured,  $\vec{\mathbb{S}}_{in}$ . This can be expressed as

$$\vec{\mathbb{S}}_{out} = M_P^H M_R(2\rho) \left[ M_R(-2\theta) M_W^V(\phi) M_R(2\theta) \right] \vec{\mathbb{S}}_{in}. \tag{13}$$

The first element of the Stokes vector  $\vec{\mathbb{S}}_{out}$  represents the total intensity of the outcoming light at each wavelength. By isolating this measurable term, we can obtain a form of the transmission modulation in terms of the biplate's properties and the initial Stokes parameters after proper algebraic manipulation, as given by

$$S'_0 = I(\theta, \phi, \rho) = \frac{1}{2} \left\{ S_0 + \frac{1}{2} (1 + \cos \phi) \left[ \cos (2\rho) S_1 + \sin (2\rho) S_2 \right] \right.$$
$$\left. + \frac{1}{2} (1 - \cos \phi) \left[ S_1 \cos (4\theta - 2\rho) \right] \right.$$
$$\left. + S_2 \sin (4\theta - 2\rho) + \sin \phi S_3 \sin (2\theta - 2\rho) \right\}. (14)$$

Equation (14) presents the theoretical model for the transmitted intensity of arbitrarily polarized light through an equivalent retarder with retardance  $\phi$  and fast axis position  $\theta$ , followed by a rotator with  $\rho$ , schemed in Fig. 4(a), and then a fixed ideal horizontal polarizer, as displayed in Fig. 2. However, it is necessary to adapt this model to account for a subtlety in the definition of the fast axis position. It has been explained that Fourier analysis-based polarimetry requires several intensities measurements of light at different retarder's fast axis positions, that is, the fast axis position is

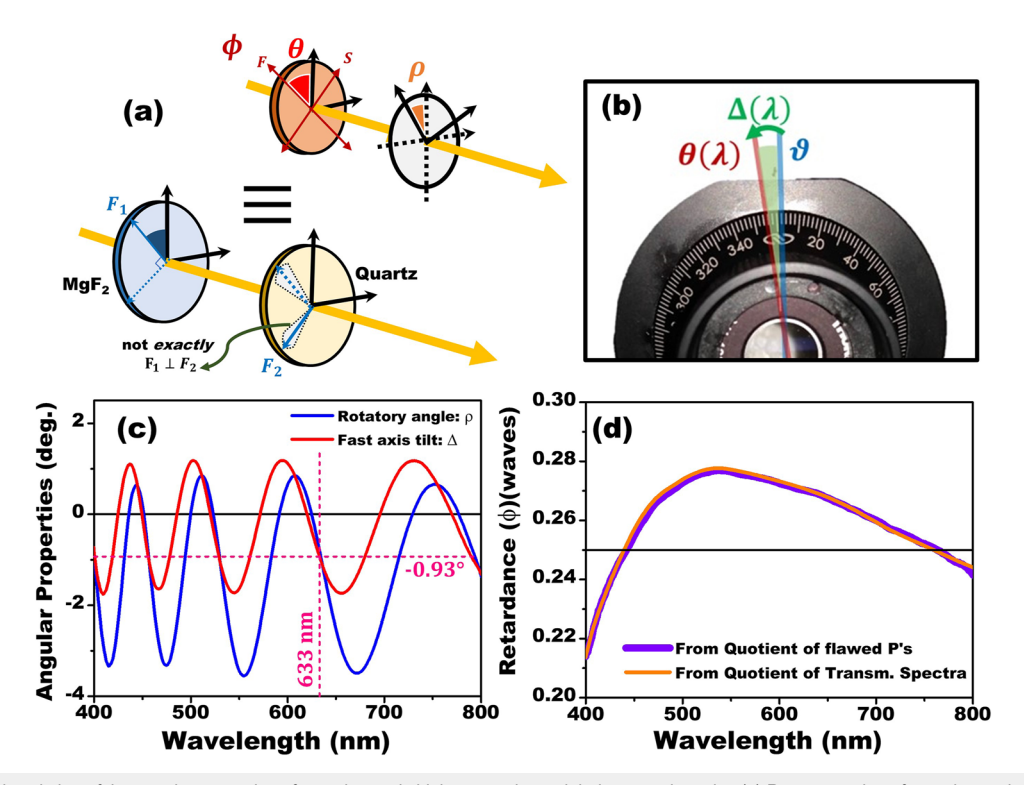


**FIG. 4.** Schematic description of the angular properties of an achromatic biplate retarder and their spectral results. (a) Representation of an achromatic retarder through the equivalence between a biplate junction and a rotated retarder with retardance  $\phi = \phi(\lambda)$  and fast axis position at  $\theta = \theta(\lambda) = \vartheta + \Delta(\lambda)$ , depicted in (b), followed by pure rotator that rotates the ellipse by  $\rho = \rho(\lambda)$ . The orange arrows indicate the direction of propagation of the incident beam, toward the detector. (c) Wavelength-dependence of angular properties: rotatory angle  $(\rho)$  in solid blue line, and fast axis tilt  $(\Delta)$  in solid red line, as well as (d) retardance in waves  $[\phi_{uaves}(\lambda) = \phi_{rad}(\lambda)/2\pi]$ , measured by both methods presented: quotient of flawed degree of polarizations (black circles) and quotient of transmission spectra (magenta solid line).

the independent variable. However, for spectral measurements, it is often assumed that the fast axis direction is the same for all wavelengths, which can be misleading. In reality, during measurements, we only have access to one fast axis mark, which is made on the mount by the manufacturer using a HeNe laser line at 633 nm as a reference. Since Eq. (14) requires  $\theta = \theta(\lambda)$  to represent the actual position of the waveplate at each wavelength  $\lambda$ , we must distinguish between what we can control (the angular position of the rotation mount in which the biplate is assembled) and what is an intrinsic dispersion of the fast axis direction, as depicted in Fig. 4(b). This distinction is described mathematically by

$$\theta$$
[ actual axis position for  $\lambda$ ] =  $\theta$ [ mark position] +  $\Delta$ [ deviation from mark for  $\lambda$ ]. (15)

Therefore, we can now express the theoretical model for modulated transmission as a function of an experimental observable, the fast axis mark's counterclockwise inclination from the vertical direction denoted as  $\vartheta$  (as in Fig. 2), and the new dispersive property of the biplate, which we shall from now on refer to as the *fast axis tilt*,  $\Delta = \Delta(\lambda)$ . Using Eq. (15), we can transform Eq. (14) into a Fourier truncated series solely in terms of the fast axis mark position. All other parameters (Stokes's and retarder's) are then encapsulated

in the amplitude terms, which are the actual measurable quantities obtained from the Fourier transform of experimental data. After the appropriate manipulations, the revised transmission modulation model is expressed as

$$I(\theta, \phi, \rho, \Delta) = \frac{1}{2} [A_0 + A_1 \cos(4\theta) + A_2 \sin(4\theta) + A_3 \sin(2\theta) + A_4 \cos(2\theta)]. \tag{16}$$

Our objective is to deduce the Stokes parameters from the amplitude terms based on our corrected biplate model. The amplitude parameters  $(A_i)$  are given by

$$A_0 = \mathbb{S}_0 + \frac{1}{2} (1 + \cos \phi) [\cos (2\rho) \mathbb{S}_1 + \sin (2\rho) \mathbb{S}_2], \tag{17a}$$

$$A_1 = \frac{1}{2} (1 - \cos \phi) [\cos (4\alpha) \mathbb{S}_1 + \sin (4\alpha) \mathbb{S}_2], \qquad (17b)$$

$$A_2 = \frac{1}{2} (1 - \cos \phi) [\cos (4\alpha) \mathbb{S}_2 - \sin (4\alpha) \mathbb{S}_1], \qquad (17c)$$

$$A_3 = \sin \phi \cos (2\beta) \mathbb{S}_3, \tag{17d}$$

$$A_4 = \sin \phi \sin (2\beta) \mathbb{S}_3, \tag{17e}$$

where  $\alpha = \Delta - \rho/2$  and  $\beta = \Delta - \rho$  are auxiliary angles. Thus, the Stokes parameters for the incoming light may be calculated from a linear combination of such amplitudes, by inverting Eq. (17), given that  $\phi(\lambda)$ ,  $\rho(\lambda)$ , and  $\Delta(\lambda)$  are known.

It is interesting to note that in contrast to the single-plate model, where  $\phi = 90^\circ$  and  $\rho = 0^\circ = \Delta$ , and only four amplitude terms were present, the new model introduces a new amplitude term,  $A_4$ , which appears only when there are non-zero angular artifacts, as given in Eq. (17e). Despite that, upon inverting these equations to isolate  $\mathbb{S}_j$  (j = 1, 2, 3), we observe that the first four amplitude terms  $A_k$  (k = 0, 1, 2, 3) are still sufficient to fully determine the Stokes parameters. Nevertheless,  $A_4$  can be useful for measuring the dispersive properties of the biplate. Before discussing the methods to characterize the properties of the biplate—the roots of the spectropolarimetric artifacts in our system—it is crucial to examine the relation between the Stokes parameters according to each model. This is important to clarify how what we have measured carried hidden quantities.

# VII. CONNECTION BETWEEN FLAWED AND TRUE PARAMETERS

Having developed a new and more complete model for estimating the Stokes parameters with a quasi-achromatic quarter-wave biplate, given by Eqs. (16) and (17), we can now establish a clear connection between the polarimetric parameters calculated with the previous and new models. Since the amplitude terms are experimentally determined from the Fourier analysis, they are model-independent. However, the way these amplitude terms depend on the Stokes parameters is model-dependent, leading us to distinguish between *flawed Stokes parameters* ( $\mathbb{Z}_1, \mathbb{Z}_2, \mathbb{Z}_3$ ) calculated from the single-plate model, and *true Stokes parameters* ( $\mathbb{S}_1, \mathbb{S}_2, \mathbb{S}_3$ ) calculated from the biplate model.

Therefore, by equating the experimentally determined amplitudes in Eq. (8) (*flawed*) and in Eq. (17) (*true*), and isolating the *flawed Stokes parameters* as functions of the *true Stokes parameters* and the waveplate's dispersive properties, we can define what we shall call the *parameter's flaw*, denoted as  $\mathbb{Z}_k/\mathbb{S}_k(k=1,2,3)$ , as

$$\mathbb{Z}_0/\mathbb{S}_0 = 1 + [s_1 \sin(2\Delta) - s_2 \cos(2\Delta)] \sin(2\beta) + [s_1 \cos(2\Delta) + s_2 \sin(2\Delta)] \cos\phi \cos(2\beta), \qquad (18a)$$

$$\mathbb{Z}_1/\mathbb{S}_1 = (1 - \cos \phi) \left[ \cos \left( 4\alpha \right) + \frac{s_2}{s_1} \sin \left( 4\alpha \right) \right], \tag{18b}$$

$$\mathbb{Z}_2/\mathbb{S}_2 = (1 - \cos \phi) \left[ \cos (4\alpha) - \frac{s_1}{s_2} \sin (4\alpha) \right], \tag{18c}$$

$$\mathbb{Z}_3/\mathbb{S}_3 = \sin \phi \cos(2\beta),$$
 (18d)

where we used that  $\alpha = \Delta - \rho/2$  and  $\beta = \Delta - \rho$ . Thus, it becomes clear from Eq. (18) how the *flawed Stokes parameters* actually carry much more information than just *real* polarimetric data from the incoming light. With this insight, we can now calculate the connection between flawed and corrected derivate parameters (e.g., degree of polarization and elliptical inclination) to corroborate the data analysis in Fig. 3(c) and 3(d).

#### A. Degree of polarization (P)

We can define the flawed ( $P_f$ ) and the true (P) degree of polarizations, according to Eq. (3), for linear polarization states, which were most frequently encountered in our experiments. The ratio between the flawed and the real degree of polarizations, referred to as the degree of polarization's flaw, provides the artifact term, which can be expressed as

$$P_f/P = \left(\sqrt{\mathbb{Z}_1^2 + \mathbb{Z}_2^2}/\mathbb{Z}_0\right) \left(\mathbb{S}_0/\sqrt{\mathbb{S}_1^2 + \mathbb{S}_2^2}\right) = (1 - \cos\phi)\mathbb{S}_0/\mathbb{Z}_0,$$
(19a)

which upon small  $\Delta$  and  $\beta$  approximations, yield

$$P_f/P \approx (1 - \cos \phi) \{1 + \cos \phi s_1 - 2[(1 - \cos \phi)\Delta - \rho]s_2\}^{-1}$$
. (19b)

Therefore, we observe that linear degree of polarization's flaw depends on intrinsic parameters of the retarder ( $\phi$  and  $\Delta$ ), as well as the initial linear polarization state ( $s_1$  and  $s_2$ ), as illustrated in Fig. 3(c). Furthermore, we find that for off-axis states, where  $s_2 \neq 0$ , a modulated dispersion in the degree of polarization can arise due to a spectrally modulated tilt of fast axis,  $\Delta(\lambda) \neq 0$ , and optical rotation,  $\rho(\lambda) \neq 0$ , which aligns with theoretical expectations from Eq. (19b). The analysis of on-axis states, which offer a promising approach for determining the biplate's effective retardance ( $\phi$ ), will be presented in Sec. VIII. It is worth highlighting that Eq. (19b) establishes how strongly the flawed degree of polarization deviates from its true values when the retarder does not present the expected  $\lambda/4$  retardance. It turns out that the flawed parameters have nothing physical, except information distorted by systemic imperfections.

### B. Elliptical inclination angle (Ψ)

We can also investigate the relationship between the *flawed* elliptical inclination  $(\psi_f)$  and the *true* elliptical inclination  $(\Psi)$  by examining their connections with associated Stokes parameters. Using Eq. (18), we find that the relationship between flawed and real elliptical inclination is given by

$$\tan (2\psi_f) = \mathbb{Z}_2/\mathbb{Z}_1 = \tan (2\Psi - 4\alpha),$$

$$\therefore \psi_f = \Psi - 2\alpha = \Psi - 2\Delta + \rho. \tag{20}$$

Thus, the *flawed* elliptical parameter measured during the simulation of states was found to be affected by two angular properties of the biplate, namely, the fast axis tilt ( $\Delta$ ) and rotatory angle ( $\rho$ ), resulting in persistent spectral undulation for all analyzed initial polarization states ( $\Psi=0^{\circ},30^{\circ},45^{\circ},60^{\circ}$ , and  $90^{\circ}$ ), including the dispersive elliptical EPL state, as exhibited in Fig. 3(d).

# VIII. MEASUREMENT OF INTRINSIC PROPERTIES OF BIPLATE RETARDERS

### A. Fast axis tilt ( $\Delta$ ) and rotatory angle ( $\rho$ )

As discussed, the truncated Fourier series in Eq. (16) fully determines the value of the amplitude parameters from experimental data, and Eq. (17) express the amplitude terms written as function of waveplate's retardance  $\phi$ , the auxiliary angles  $\alpha$  and  $\beta$ , and the Stokes parameters of incoming light. Our goal now is to establish a

clear procedure to determine the retarder's angular dispersive properties  $(\phi, \rho, \Delta)$  by controlling the polarization state of the incoming light beam,  $(\mathbb{S}_1, \mathbb{S}_2, \mathbb{S}_3)$ . In Eq. (17), we observe four experimentally-determined quantities that depend on equal terms in pairs, which immediately leads to the following relationship:

$$A_{2}/A_{1} = \frac{\left[\mathbb{S}_{2} \cos(4\alpha) - \mathbb{S}_{1} \sin(4\alpha)\right]}{\left[\mathbb{S}_{1} \cos(4\alpha) + \mathbb{S}_{2} \sin(4\alpha)\right]} = \tan(2\Psi - 4\alpha), \quad (21a)$$

$$A_4/A_3 = \tan(2\beta). \tag{21b}$$

Equation (21a) has been previously discussed in Sec. VII B as a connection between flawed and real elliptical inclination, but now it is explicitly written in terms of the amplitude parameters and the incoming polarization state. It is worth noting that for an on-axis VPL state, for which  $\mathbb{S}_1 \neq 0$  and  $\mathbb{S}_2 = 0$ , the equation can be conveniently simplified to

$$A_2/A_1 = -\tan(4\alpha), \tag{22}$$

which directly determines the auxiliary angle  $\alpha = \Delta - \rho/2$ . Meanwhile, Eq. (21b) already establishes a direct connection between two amplitude terms and the other auxiliary angle,  $\beta = \Delta - \rho$ . Nevertheless, it should be noted that Eq. (21b) is only well-defined for incoming light states where  $\mathbb{S}_3 \neq 0$ , that is, any non-linear polarization state.

Therefore, given the appropriate initial polarization state, we can determine both auxiliary angles directly from the amplitude terms after two different experiments, as given by

$$\tan(4\alpha) = -A_2/A_1,\tag{23a}$$

$$\tan(2\beta) = A_4/A_3 \tag{23b}$$

such that  $\alpha$  can be determined from Eq. (23a) in a measurement of VPL, and  $\beta$ , from Eq. (23b), in an experiment involving a *non-linearly* polarized light, that is, a state with  $\mathbb{S}_3 \neq 0$ . Thus, from two simple rounds of experiments, the auxiliary angles can be determined using Eqs. (23a) and (23b), and the intrinsic properties can then be obtained as

$$\rho = 2(\alpha - \beta),\tag{24a}$$

$$\Delta = 2\alpha - \beta. \tag{24b}$$

Notice that if  $\rho=0$ , then  $\alpha=\beta$ , for all wavelengths detected. If they are different, that should be an experimental corroboration of our new approach. For our measurements, we utilized a calcite crystal as vertical polarizer, set up by adjusting its transmission axis with analyzer's until they are crossed and then minimum transmission spectrum is reached, to ensure  $\mathbb{S}_2=0$  and  $\mathbb{S}_1=-1$  for determining  $\alpha$ . Subsequently, to determine  $\beta$ , we employed the circular polarizer filter presented in Sec. IV, as it maintains the requirement of  $\mathbb{S}_3\neq 0$  across the entire visible spectrum.

Our spectral experimental results obtained from Eq. (24) are presented in Fig. 4(c). As depicted, the dispersion of the biplate's intrinsic angular properties, namely, the rotatory angle (blue solid line) and fast axis tilt (red solid line), exhibit shifted undulated spectral distributions, asymmetric around zero, with varying amplitudes, indicating that they are indeed two distinct and non-negligible

properties. Nevertheless, the amplitudes of the waveforms presented in this section are sufficiently small to support the assumptions for approximations of utilized in Sec. VII A, although none were used in the data processing of the software.

It is important to make clear that, although the undulated wavelength-dependence of the fast axis tilt is well determined with this method, the overall level of the red curve shown in Fig. 4(c) is highly dependent on the accurate positioning of the mounted retarder crystal's fast axis engraving, given by manufacturers, to the vertical 0° mark of the rotation mount. Since  $\Delta(\lambda)$  quantifies how much the real fast axis position of the biplate retarder at a particular wavelength is shifted (or tilted) from the overall fast axis, given experimentally by  $\vartheta$ , the tilt value of zero is expected to be of the wavelength for which the waveplate's engraving was initially designated. Hence, despite being a modulated dispersion, the fast axis tilt curve has no physical reason to be symmetric around zero, but cross this level at the calibration wavelength, at 633 nm.

In Fig. 4(c), we observe an angular shift of about  $-0.93^{\circ}$  on the fast axis tilt level at 633 nm, which is within our manual accuracy to assemble and align the engraved fast axis of the mounted retarder with the  $0^{\circ}$  mark of the rotation mount. Notice that without an external reference from which we can establish a relative fast axis for each wavelength, the absolute values of the fast axis tilt wavelength-dependence could not be determined, and a symmetrical distribution could be constructed as reference. The slight overall shift of  $-0.93^{\circ}$  in the fast axis tilt was maintain in posterior data analysis to account for the initial crystal misalignment, without compromising the reliability of the troubleshooting protocol developed in this work.

### B. Retardance ( $\phi$ )

### 1. Quotient of flawed degree of polarizations

In Sec. VII A, we evaluated the *degree of polarization's flaw*, which is the ratio between the flawed and real degree of polarizations ( $P_f$  and P) for an arbitrary Linearly Polarized Light (LPL), as given by Eq. (18). As shown, for a HPL, where ( $s_1, s_2, s_3$ ) = (+1,0,0), and a VPL, where ( $s_1, s_2, s_3$ ) = (-1,0,0), Eq. (18) yields Eqs. (25a) and (25b), respectively,

$$P_f^H/P^H = \frac{(1-\cos\phi)}{(1+\cos\phi)},$$
 (25a)

$$P_f^V/P^V = \frac{(1-\cos\phi)}{(1-\cos\phi)} = 1.$$
 (25b)

Since rotating the polarizer has no physical reason to polarize a different fraction of light, the correct degree of polarization values ( $P^H$  and  $P^V$ ) should be the same for linear states generated with the same polarizer. Thus, we can assume that the correct values are equivalent, that is,  $P^H = P^V$ . Therefore, the ratio of degree of polarization's flaws measured for HPL and VPL yields

$$P_f^H / P_f^V = \frac{1 - \cos \phi}{1 + \cos \phi}.$$
 (26)

Isolating the retardance term, we obtain a direct manner to obtain the retardance spectrum from flawed dispersions of degree of polarization of two orthogonal polarization states

$$\cos \phi = \frac{P_f^V - P_f^H}{P_f^V + P_f^H}.$$
 (27)

Hence, as predicted in Eq. (25b), the data in Fig. 3(c) for the flawed degree of polarization of VPL indicated how the degree of polarization should be for all linear states generated with the same polarizer: flawless, that is, without spectral modulation and above-unity issues. Conversely, as demonstrated in Eq. (27), the deviation of the flawed degree of polarization for HPL  $(P_f^H)$  from the correct value  $(P_f^V = P^V)$  indicates a direct manifestation of the non-achromaticity from our retarder, initially assumed achromatic in the range from 400 to 800 nm. For instance, in the range in which  $P_f^H \neq 1$ , we expect  $\phi/2\pi \neq 0.25$ . It is noteworthy that the fact we can obtain all three dispersive parameters from the calibration data of simulated states demonstrate self-consistency, as well as a powerful advantage for this kind of setup to be applied in spectropolarimetry. The experimental result from this method is displayed in Fig. 4(d), compared with the method of quotient of transmission spectra, which is described as a quicker experimental alternative as follows.

### 2. Quotient of transmission spectra

For the second method, we can once again utilize Eqs. (16) and (17). Besides representing the modulation of transmission intensity over retarder's rotation given an arbitrarily polarized beam, this truncated Fourier series is also valid for a setup where the incoming light is changed at will, and the retarder is fixed at an angle  $\vartheta$  from the vertical position. In other words, the same model can be used to describe a setup in which the retarder is placed at a particular angle from the vertical between two polarizers (the first, a polarization controller, and the second, our fixed horizontal analyzer).

In this sense, the amplitude parameters provided in Eq. (17) can be conveniently applied to an incoming light either HPL, for which  $(s_1, s_2, s_3) = (+1, 0, 0)$  or VPL, for which  $(s_1, s_2, s_3) = (-1, 0, 0)$ . Notice that for each of these conditions, Eqs. (16) and (17) yield Eq. (28)

$$I^{HH}(\vartheta) = \frac{\mathbb{S}_0}{2} \left[ 1 + \frac{\left( 1 + \cos \phi \right)}{2} \cos \left( 2\rho \right) + \frac{\left( 1 - \cos \phi \right)}{2} \cos \left( 4\vartheta + 4\alpha \right) \right], \tag{28a}$$

$$I^{VH}(\vartheta) = \frac{\mathbb{S}_0}{2} \left[ 1 - \frac{\left( 1 + \cos \phi \right)}{2} \cos \left( 2\rho \right) - \frac{\left( 1 - \cos \phi \right)}{2} \cos \left( 4\vartheta + 4\alpha \right) \right]. \tag{28b}$$

Here, they represent the spectrum of transmitted light through the retarder rotated counterclockwise by  $\vartheta$  placed between polarizers being either parallel ( $I^{HH}$ : polarizer at H and analyzer at H) or perpendicular ( $I^{VH}$ : polarizer at V and analyzer at H) to each other.

Now, it is defined the quantity so-called *quotient of transmission spectra* (Q) as

$$Q(\theta) = \frac{I^{HH}(\theta) - I^{VH}(\theta)}{I^{HH}(\theta) + I^{VH}(\theta)},$$
(29)

which may be obtained from Eqs. (28a) and (28b) as a function of retarder's parameters only, as

$$Q(\theta) = \frac{(1 + \cos\phi)}{2}\cos(2\rho) + \frac{(1 - \cos\phi)}{2}\cos(4\theta + 4\alpha). \quad (30)$$

For small  $\rho$  [see Fig. 4(c)], we can use  $\cos(2\rho) \approx 1$  such that Eq. (30) simplifies to

$$Q(\theta) = 1 - (1 - \cos \phi)\sin^2(4\theta + 4\alpha), \tag{31}$$

which can then be applied for specific angular positions  $\vartheta$ . Note that for  $\vartheta=0^\circ$  and  $\vartheta=45^\circ$ , we obtain

$$Q(0^{\circ}) = 1 - (1 - \cos \phi)\sin^2(4\alpha),$$
 (32a)

$$Q(45^{\circ}) = 1 - (1 - \cos \phi)\cos^2(4\alpha).$$
 (32b)

Hence,

$$\cos \phi = Q(45^{\circ}) + Q(0^{\circ}) - 1. \tag{33}$$

Therefore, Eq. (33) provides a convenient method to measure the retardance spectrum  $\phi = \phi(\lambda)$  by acquiring only four spectra. This is because calculating each  $Q(\vartheta)$  requires the use of two transmission spectra: one with retarder between parallel polarizers ( $I^{HH}$ ), and another with the retarder placed between perpendicular polarizers ( $I^{VH}$ ). Notice that  $1-Q(0^{\circ})$  should approach zero, once a retarder at  $\vartheta=0^{\circ}$  (vertical) would make either HPL or VPL cross through only one of birefringent retarder's index of refraction. However, as demonstrated previously, the biplate does not interact with all wavelengths of light the same way, causing deviations from the expected  $1-Q(0^{\circ})=0$  throughout the spectrum. This term should then account for these deviations as fine tuning for the  $Q(45^{\circ})$  term. For the situation that  $1-Q(0^{\circ})$  is negligibly small, we obtain a final approximation as

$$\cos \phi = Q(45^{\circ}) = \frac{I^{HH}(45^{\circ}) - I^{VH}(45^{\circ})}{I^{HH}(45^{\circ}) + I^{VH}(45^{\circ})},$$
 (34)

which looks quite similar in structure to the model from the method of *quotient of flawed degree of polarizations*, in Eq. (27), and is a well-known version of method to acquire the retardance value of a retarder at a particular wavelength. <sup>18,69</sup>

The experimental data of retardance evaluated by both methods presented in this section are shown in Fig. 4(d), in waves unit. The violet curve shows the result for the *quotient of flawed degree of polarizations*, acquired according to Eq. (27), by making use of the flawed data generated with the single-plate model for vertical and horizontally polarized light. Such polarization states were created by a careful alignment of the calcite polarizer to the vertical by crossing it with the analyzer at horizontall, and it was then rotated by 90° in a rotation mount to set it horizontally. The orange curve displays the average of four measurements of *quotient of transmission spectra's* results, obtained according to Eq. (33). The error bars were omitted for such since they were about the size of line thickness.

It is noticeable how similar both curves are which validates the equivalence between both methods with slightly different approaches. Besides, the horizontal black line at the 0.25 waves level

marks the *quarter-wave plate* ideal behavior, thereby making explicit the *quasi-achromatic* behavior of our retarder, with  $\pm 0.03$  waves ( $\pm 12\%$ ) of variation from the ideal case.

Moreover, the results obtained through Eq. (34) are not displayed here due to the  $1-Q(0^\circ)$  term not being negligible in our case. Notice that  $1-Q(0^\circ)\approx 0$  only happens when  $I^{VH}(0^\circ)\approx 0$  throughout the spectrum, which could not be seen in Fig. 3(b), where the green curve, which essentially means  $I^{VH}(0^\circ,\lambda)$ , does not match with crossed-polarizers intensity level along the detected range. In fact, if not considered, this approximation causes a slightly modulation throughout the retardance spectrum, which is fully attenuated when considered. After all the biplate's intrinsic parameters being fully measured, the correct calculations of the Stokes parameters, by inverting Eq. (17), were implemented in a MATLAB program, and the data presented in Figs. 4(c) and 4(d) were saved as *calibration curves* for all future experiments and data correction of old ones.

# IX. EFFECTS OF BIPLATE MODEL ON POLARIMETRIC DATA

Next, the corrected biplate model developed above was applied to calculate the Stokes parameters of the same generated polarization states displayed in Figs. 3(c) and 3(d). The experimental method employed was the precisely the same as described in Sec. IV. The polarimetric data are shown in Fig. 5. In Figs. 5(a) and 5(b), we present the comparisons for two off-axis linear states (45° and 30°

linearly polarized states, respectively) of true  $(s_k = \mathbb{S}_k/\mathbb{S}_0, k = 1, 2, 3, in solid lines)$  and flawed  $(z_k = \mathbb{Z}_k/\mathbb{Z}_0, k = 1, 2, 3, in faded lines)$  Stokes total-fractions, which, respectively, means the data generated with the corrected biplate model and with the single-plate model. More of such comparison for other polarization states can be found in Sec. S3 of the supplementary material. In Figs. 5(c) and 5(d), we exhibit the corrected version of the dispersions of degree of polarization (P) and elliptical inclination ( $\Psi$ ), previously displayed in Figs. 3(c) and 3(d), where we can clearly evaluate that previous spectral artifacts as signs of inadequate model are largely eliminated when utilizing the biplate model.

In Fig. 5(a), the comparison of true and flawed Stokes totalfractions for 45° linearly polarized light is presented. The dashed red line representing the  $z_1 = \mathbb{Z}_1/\mathbb{Z}_0$  curve was above unity and strongly modulated, causing the associated degree of polarization to have the same problem, as previously exhibited as a solid blue line in Fig. 3(c). After correction of the single-plate model, the solid red line representing the  $s_1 = S_1/S_0$  curve was accurately estimated to be nearly at 1 throughout the whole spectrum. Additionally, the faded blue line representing the  $z_2 = \mathbb{Z}_2/\mathbb{Z}_0$  curve presented a strong wave-like pattern that resulted in the modulation seen in the elliptical inclination dispersion, previously shown as a solid blue line in Fig. 3(d), which was attenuated in  $s_2 = \mathbb{S}_2/\mathbb{S}_0$ . solid blue line curve of Fig. 5(a). The  $z_3 = \mathbb{Z}_3/\mathbb{Z}_0$  and  $s_3 = \mathbb{S}_3/\mathbb{S}_0$  curves (faded and solid green lines, respectively) are quite similar since both are too close to zero in this range, which is expected for linear polarization states.

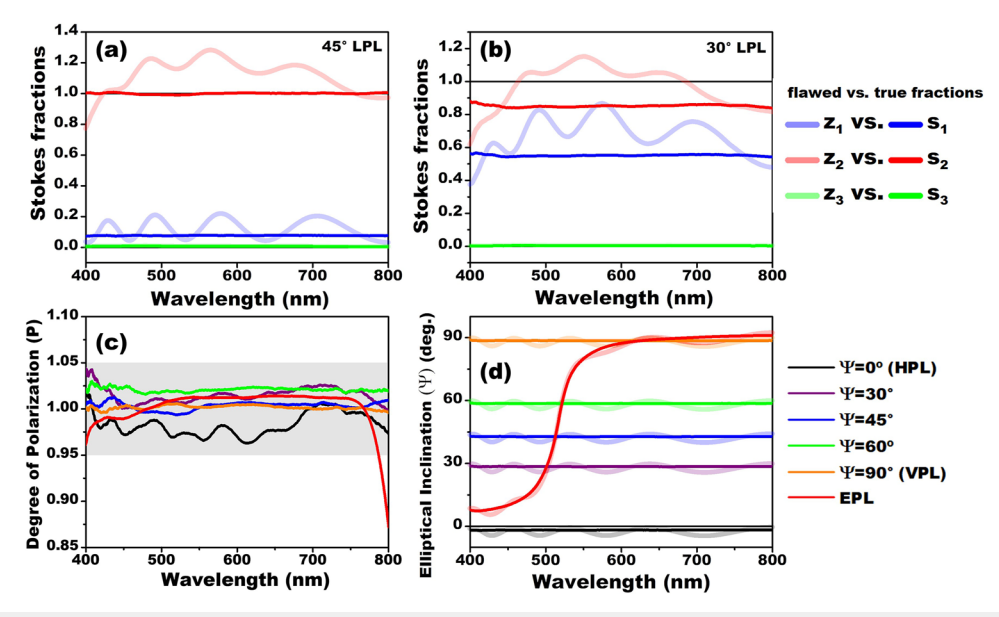


FIG. 5. Polarimetric results calculated with the proposed biplate model from experimental data acquired with broadband controllable polarized light. (a) Plot of true Stokes total-fractions ( $\mathbf{s}_k = \mathbb{S}_k/\mathbb{S}_0$ ,  $\mathbf{k} = 1, 2, 3$ ), in solid lines, superposed with flawed total-fractions ( $\mathbf{z}_k = \mathbb{Z}_k/\mathbb{Z}_0$ ,  $\mathbf{k} = 1, 2, 3$ ), in faded lines, for 45° Linearly Polarized Light (LPL). (b) Plot of true Stokes total-fractions, in bright solid lines, superposed with flawed total-fractions, in faded lines, for 30° LPL. The plots for the remaining polarization states are available in Sec. S3 of the supplementary material. (c) Plot of degree of polarization spectra [ $\mathbf{P}(\lambda)$ ], estimated from the true Stokes parameters, calculated with the biplate model for different incoming polarization states: from  $\mathbf{\Psi} = 0^\circ$  (HPL) to  $\mathbf{\Psi} = 90^\circ$  (VPL), and EPL, the overall elliptical state. The gray shadowed area shows that the new results fit within  $\pm 5^\circ$  accuracy from unity. (d) Plot of elliptical inclination spectra [ $\mathbf{\Psi}(\lambda)$ ], in degrees, for six incoming polarization states. The curves estimated from the true Stokes parameters, calculated with the biplate model, are displayed as bright solid lines, and the flawed curves, estimated from the flawed Stokes parameters, calculated with the same color as their true counterparts.

In Fig. 5(b), the comparison is now made for 30° linearly polarized light, and we can see similar patterns disappearing with the use of the biplate model. It is important to note that although  $z_1$ and  $z_2$  are not above unity, together they contribute to the associated degree of polarization being above unity, as previously shown in Fig. 3(c) as a solid purple line. In addition, they both show intense spectral undulation, which leads to a modulated elliptical inclination dispersion, as depicted in Fig. 3(d) as a solid purple line. All these artifacts were effectively eliminated with the implementation of the new model. Figure 5(c) shows the corrected degree of polarization dispersions for six different polarization states, which should be directly compared to Fig. 3(c) for a better appreciation of how the new model solved previous artifact issues, as now the curves no longer exceed 1, and both on- and off-axis polarization states are similar, without any spectral modulations for the off-axis ones. The gray area highlights the range of values within 5% deviation from a unitary degree of polarization, which is an acceptable theoretical reference due to the high polarizing capacity of our linear polarizer (see Sec. S2.1 of the supplementary material). As expected, the rotation of the polarizer has no physical reason to change the degree of polarization of light, even though it changes its state. Additionally, the inset provides a closer look at the curves within the same range, and we see that they do not match exactly, with slight modulations for  $\Psi = 0^{\circ}$ and 30°, and a deviation slightly above one for other states. However, in contrast to the curves in Fig. 3(c), these deviations are greatly smaller for the corrected data, with values mostly in the  $\pm 2\%$  range of deviation from expected unity, which can be considered negligible. Hence, we can conclude that the biplate model appropriately accounts for the spectral artifacts shown in Fig. 3(c).

Finally, for a better appreciation of the improvements achieved, Fig. 5(d) displays the direct comparison of corrected (bright solid lines) and flawed (faded solid lines) dispersions of the elliptical inclination angle for the same polarization states as in Fig. 3(d). The corrected curves show a remarkable enhancement in smoothness, with almost complete attenuation of the spectral modulation for all analyzed states. Even the curve for the circular filter (solid red line), which exhibits a larger overall change in the elliptical inclination angle along the wavelength range, exhibits a conspicuous smoothing effect. However, it is important to highlight that the small deviation from the targeted elliptical inclination of  $\sim 2^{\circ}$ , observable for the linear states in Fig. 3(d), may be attributed to a slight misalignment between the calcite polarizer and the rotation mount, which is within our manual rotation precision and does not affect the intended analysis approach of this work. What in Fig. 3(d) appeared to be only slight oscillations in the spectrum, is now clarified to be mostly caused by the intrinsic properties of the biplate, whereas the overall level of each curve was determined by the initial alignment precision of the calcite polarizer.

Overall, the results demonstrate that the single-plate model does not recover the experimental findings. In fact, the flawed data contained more information than the true Stokes parameters, and this excess of information was avoided with the proposed biplate model.

#### X. CONCLUSION AND OUTLOOK

In this study, we demonstrate that the model typically presented in books for measuring Stokes parameters via rotating retarder

polarimetry and Fourier analysis of transmitted signals cannot be directly used for spectral applications. We show that the use of quasiachromatic biplate retarders requires further calibration, as they strongly depend on the birefringent properties of materials, majorly dispersive over the light spectrum. We also demonstrate that probing the spectral distributions of Stokes parameters with a simulation system of broadband polarization states is sufficient to observe how the simplest model propagates the artifacts from the quarter-wave retarder. The model typically employed in single-wavelength applications has flaws when considered carelessly as valid for polychromatic light sources. We show that the Stokes parameters calculated using the single-plate model incorporate the intrinsic properties of the biplate retarder into the polarimetric data. Supported by *Jones*' optical equivalence theorem, we develop a new model that considers the biplate nature of imperfect quasi-achromatic retarders and their properties [retardance ( $\phi$ ), fast-axis tilt ( $\Delta$ ), and rotatory angle ( $\rho$ )] that can be measured and saved as calibration files used to improve the accuracy of the experiment during data processing.

We anticipate that this spectropolarimetric model can be applied to different situations. Either from transmission or emission, the tracking of changes in polarization states due to interaction with materials can be a powerful tool for investigating anisotropic properties, 5,10,70 such as linear and circular birefringence (also known as optical activity), linear and circular dichroism, and partially polarized photoemission and scattering from conjugated organic molecules.<sup>55,71–77</sup> The latter is of particular interest in organic electronics owing to its potential for supramolecular arrangements and film deposition, as well as its charge transport properties. Although many studies have utilized spectral versions of Stokes polarimetry, they tend to render the single-wavelength model applicable to non-ideal optical elements without proper polychromatic calibration protocols or model correction. Therefore, this study contributes to this field by providing a detailed account of the mathematical and experimental procedures to improve both data analysis and precision in Stokes spectropolarimetry experiments. Alternatively, the possibility of applications in the investigation of simple systems, such as the optical activity of aqueous solutions of different sugars and the linear birefringence of stretched sticky tapes, may be potentially utilized to introduce interested undergraduate students to this field. From this perspective, such applications present themselves as a great pedagogical option for young scientists to learn how to use light polarization to probe anisotropic phenomena. Finally, since the light interacts with matter in many different scales of time and space, the methodology presented here could be extended to the analysis of the polarization state of light in time-resolved experiments (timeresolved polarimetry) and confocal microscopy (space-resolved polarimetry).

#### SUPPLEMENTARY MATERIAL

The supplementary material presents supporting content on the Mueller matrices of polarizing elements (linear polarizer, linear retarder, rotator, and rotated elements), independent efficiency measurements of linear polarizer, influence of acquisition controls on data precision, and direct comparison of polarimetric data generated with single- and biplate models.

#### **ACKNOWLEDGMENTS**

The authors are indebted to the following Brazilian agencies: Conselho Nacional de-Desenvolvimento Científico e Tecnológico CNPq under Grant Nos. 306147/2020-3 and 465572/2014-6, São Paulo Research Foundation (FAPESP) (Grant No. 2014/50869-6), CAPES (Education Ministry) (Grant No. 23038.000776/201754) via projects of the National Institute for Science and Technology on Organic Electronics (INEO), FAPESPA and CAPES under Grant Nos. Finance Code 001 and AUXPE 88881.159129/2017-01. P.T.A. is especially grateful to the National Science Foundation (NSF) under Grant No. 1848418 for financial support. N.M.B.N. is especially grateful to Fulbright Foundation for the Visiting Professor Scholarship Award. The authors are grateful to Professor Sanclayton Moreira from the Graduate Program in Physics of the Federal University of Para for granting access to his experimental facilities.

#### **AUTHOR DECLARATIONS**

#### **Conflict of Interest**

The authors have no conflicts to disclose.

#### **Author Contributions**

Ruan L. S. Lima: Conceptualization (equal); Data curation (equal); Formal analysis (equal); Investigation (equal); Methodology (equal); Writing – original draft (equal); Writing – review & editing (equal). Paulo T. Araújo: Data curation (equal); Funding acquisition (equal); Project administration (equal); Resources (equal); Supervision (equal); Validation (equal); Writing – review & editing (equal). Newton M. Barbosa Neto: Conceptualization (equal); Data curation (equal); Formal analysis (equal); Funding acquisition (equal); Investigation (equal); Methodology (equal); Project administration (equal); Resources (equal); Supervision (equal); Validation (equal); Visualization (equal); Writing – original draft (equal); Writing – review & editing (equal).

### **DATA AVAILABILITY**

Data underlying the results presented in this paper are not publicly available at this time, but may be obtained from the corresponding author upon reasonable request.

#### **REFERENCES**

<sup>1</sup> P. C. Brady, A. A. Gilerson, G. W. Kattawar, J. M. Sullivan, M. S. Twardowski, H. M. Dierssen, M. Gao, K. Travis, R. I. Etheredge, A. Tonizzo, A. Ibrahim, C. Carrizo, Y. Gu, B. J. Russell, K. Mislinski, S. Zhao, and M. E. Cummings, "Open-ocean fish reveal an omnidirectional solution to camouflage in polarized environments," Science 350(6263), 965–969 (2015).

<sup>2</sup>Y. L. Gagnon, R. M. Templin, M. J. How, and N. J. Marshall, "Circularly polarized light as a communication signal in Mantis shrimps," Curr. Biol. **25**(23), 3074–3078 (2015).

<sup>3</sup>M. J. How, J. H. Christy, S. E. Temple, J. M. Hemmi, N. J. Marshall, and N. W. Roberts, "Target detection is enhanced by polarization vision in a fiddler crab," Curr. Biol. 25(23), 3069–3073 (2015).

<sup>4</sup>G. Horváth, *Polarized Light and Polarization Vision in Animal Sciences* (Springer, Berlin, Heidelberg, 2014).

- <sup>5</sup>N. Ghosh, "Tissue polarimetry: Concepts, challenges, applications, and outlook," J. Biomed. Opt. **16**(11), 110801 (2011).
- <sup>6</sup> J. Xuan, U. Klimach, H. Zhao, Q. Chen, Y. Zou, and Y. Wang, "Improved diagnostics using polarization imaging and artificial neural networks," Int. J. Biomed. Imaging 2007, 074143 (2007).
- <sup>7</sup>E. Costa, P. Soffitta, R. Bellazzini, A. Brez, N. Lumb, and G. Spandre, "An efficient photoelectric x-ray polarimeter for the study of black holes and neutron stars," Nature 411(6838), 662–665 (2001).
- <sup>8</sup> A. M. Anile and R. A. Bruer, "Gravitational Stokes parameters," Astrophys. J. 189, 39 (1974).
- <sup>9</sup>F. Snik and C. U. Keller, *Planets, Stars and Stellar Systems* (Springer Netherlands, Dordrecht, 2013), pp. 175–221.
- <sup>10</sup>L. Rossi, J. Berzosa-Molina, J.-M. Desert, L. Fossati, A. G. Muñoz, C. Haswell, P. Kabath, K. Kislyakova, D. Stam, A. Vidotto, D. Stam, and M. S. Nl, "Spectropolarimetry as a tool for understanding the diversity of planetary atmospheres," Exp. Astron. 54, 1187–1196 (2022).
- <sup>11</sup> J. Bonnel, J. Flamant, D. R. Dall'Osto, N. Le Bihan, and P. H. Dahl, "Polarization of ocean acoustic normal modes," J. Acoust. Soc. Am. 150(3), 1897–1911 (2021).
- <sup>12</sup>M. F. Sterzik, S. Bagnulo, and E. Palle, "Biosignatures as revealed by spectropolarimetry of Earthshine," Nature **483**(7387), 64–66 (2012).
- <sup>13</sup>K. A. Hart, M. Kupinski, D. Wu, and R. A. Chipman, "First results from an uncooled LWIR polarimeter for cubesat deployment," Opt. Eng. **59**(07), 075103 (2020).
- <sup>14</sup>M. Losurdo, M. Bergmair, G. Bruno, D. Cattelan, C. Cobet, A. de Martino, K. Fleischer, Z. Dohcevic-Mitrovic, N. Esser, M. Galliet, R. Gajic, D. Hemzal, K. Hingerl, J. Humlicek, R. Ossikovski, Z. V. Popovic, and O. Saxl, "Spectroscopic ellipsometry and polarimetry for materials and systems analysis at the nanometer scale: State-of-the-art, potential, and perspectives," J. Nanopart. Res. 11(7), 1521–1554 (2009).
- 15 Y. Liang, H. Lin, K. Koshelev, F. Zhang, Y. Yang, J. Wu, Y. Kivshar, and B. Jia, "Full-Stokes polarization perfect absorption with diatomic metasurfaces," Nano Lett. 21(2), 1090–1095 (2021).
- <sup>16</sup>R. A. Chipman, W.-S. T. Lam, and G. Young, Polarized Light and Optical Systems, Optical Sciences and Applications of Light (CRC Press; Taylor and Francis, Boca Raton, 202018).
- <sup>17</sup>H. Fujiwara, Spectroscopic Ellipsometry (Wiley, 2007).
- <sup>18</sup>D. H. Goldstein, *Polarized Light* (CRC Press, 2017).
- <sup>19</sup>W. Ke and J. Wu, "Polarization response of the grating monochromator and the effect of optical installation on spectral measurement," in *Proceedings of the International Conference on Holography and Optical Information Processing* (SPIE 2017), Vol. 2866, pp. 439–442.
- <sup>20</sup>J. R. Lakowicz, *Principles of Fluorescence Spectroscopy* (Springer US, Boston, MA, 2006).
- H. G. Berry, G. Gabrielse, and A. E. Livingston, "Measurement of the Stokes parameters of light," Appl. Opt. 16(12), 3200 (1977).
   P. Alliprandini-Filho, R. A. da Silva, N. M. Barbosa Neto, and A. Marletta,
- <sup>22</sup>P. Alliprandini-Filho, R. A. da Silva, N. M. Barbosa Neto, and A. Marletta, "Partially polarized fluorescence emitted by MEHPPV in solution," Chem. Phys. Lett. **469**(1–3), 94–98 (2009).
- <sup>23</sup>P. Alliprandini-Filho, G. B. da Silva, N. M. Barbosa Neto, R. A. Silva, and A. Marletta, "Induced secondary structure in nanostructured films of poly(p-phenylene vinylene)," J. Nanosci. Nanotechnol. 9(10), 5981–5989 (2009).
- <sup>24</sup>P. Alliprandini-Filho, G. F. Borges, W. B. Calixto, I. H. Bechtold, A. A. Vieira, R. Cristiano, H. Gallardo, R. A. Silva, N. B. Neto, and A. Marletta, "Molecular alignment effects on spectroscopic properties 2,1,3-benzothiadiazole guested in liquid-crystalline compounds," Chem. Phys. Lett. 487(4–6), 263–267 (2010).
- <sup>25</sup>P. Alliprandini-Filho, R. A. Silva, G. B. da Silva, N. M. B. Neto, L. A. Cury, R. L. Moreira, and A. Marlleta, "Measurement of the emitted light polarization state in oriented and non-oriented PPV films," Macromol. Symp. **245–246**(1), 406–409 (2006)
- <sup>26</sup>P. Alliprandini Filho, G. G. Dalkiranis, R. A. S. Z. Armond, E. M. Therézio, I. H. Bechtold, A. A. Vieira, R. Cristiano, H. Gallardo, A. Marletta, and O. N. Oliveira, "Emission ellipsometry used to probe aggregation of the luminescent 2,1,3-benzothiadiazole dyes and ordering in an E7 liquid crystal matrix," Phys. Chem. Chem. Phys. 16(7), 2892 (2014).
- <sup>27</sup>E. M. Therézio, P. C. Rodrigues, J. R. Tozoni, A. Marletta, and L. Akcelrud, "Energy-transfer processes in donor-acceptor poly (fluorenevinylene- alt

- -4,7-dithienyl-2,1,3-benzothiadiazole)," J. Phys. Chem. C 117(25), 13173-13180
- <sup>28</sup>E. M. Therézio, F. Franchello, I. F. L. Dias, E. Laureto, M. Foschini, O. L. Bottecchia, H. de Santana, J. L. Duarte, and A. Marletta, "Emission ellipsometry as a tool for optimizing the electrosynthesis of conjugated polymers thin films," Thin Solid Films 527, 255-260 (2013).
- <sup>29</sup> M. L.-N. Phan, M. N. Nguyen, and H. T.-T. Pham, in *IFMBE Proceedings*, edited by V. van Toi, T. Le, H. Ngo, and T. H. Nguyen (Springer, Singapore, 2020), Vol. 69, pp. 427-432.
- 30 T. A. Wilkinson, C. E. Maurer, C. J. Flood, G. Lander, S. Chafin, and E. B. Flagg, "Complete Stokes vector analysis with a compact, portable rotating waveplate polarimeter," Rev. Sci. Instrum. **92**(9), 093101 (2021).

  <sup>31</sup> R. M. A. Azzam, "Photopolarimetric measurement of the Mueller matrix by
- Fourier analysis of a single detected signal," Opt. Lett. 2(6), 148 (1978).
- 32 R. M. A. Azzam, "Mueller-matrix ellipsometry: A review," Proc. SPIE 3121, 396
- 33 R. M. A. Azzam, "Stokes-vector and Mueller-matrix polarimetry (invited)," J. Opt. Soc. Am. A 33(7), 1396 (2016).
- <sup>34</sup>P. S. Hauge, "Mueller matrix ellipsometry with imperfect compensators," J. Opt. Soc. Am. 68(11), 1519 (1978).
- <sup>35</sup>A. Laskarakis, S. Logothetidis, E. Pavlopoulou, and M. Gioti, "Mueller matrix spectroscopic ellipsometry: Formulation and application," Thin Solid Films 455-456, 43-49 (2004).
- $^{\bf 36}\mbox{S}.$  Liu, X. Chen, and C. Zhang, "Development of a broadband Mueller matrix ellipsometer as a powerful tool for nanostructure metrology," Thin Solid Films 584, 176-185 (2015).
- <sup>37</sup>X. Chen, H. Gu, J. Liu, C. Chen, and S. Liu, "Advanced Mueller matrix ellipsometry: Instrumentation and emerging applications," Sci. China Technol. Sci. 65(9), 2007-2030 (2022).
- <sup>38</sup>H. G. Tompkins and J. N. Hilfiker, Spectroscopic Ellipsometry: Practical Application to Thin Film Characterization (Momentum Press, New York, 2016).
- <sup>39</sup>D. H. Goldstein and R. A. Chipman, "Error analysis of a Mueller matrix polarimeter," J. Opt. Soc. Am. A 7(4), 693 (1990).
- <sup>40</sup>D. H. Goldstein, "Mueller matrix dual-rotating retarder polarimeter," Appl. Opt. 31(31), 6676 (1992).
- <sup>41</sup>R. D. Hawley, J. Cork, N. Radwell, and S. Franke-Arnold, "Passive broadband full Stokes polarimeter using a Fresnel cone," Sci. Rep. 9(1), 2688 (2019).
- <sup>42</sup>L. Giudicotti and M. Brombin, "Data analysis for a rotating quarter-wave, farinfrared Stokes polarimeter," Appl. Opt. 46(14), 2638 (2007).
- <sup>43</sup>C. Flueraru, S. Latoui, J. Besse, and P. Legendre, "Error analysis of a rotating quarter-wave plateplate Stokes' polarimeter," IEEE Trans. Instrum. Meas. 57(4), 731-735 (2008).
- <sup>44</sup>H. Dong, M. Tang, and Y. Gong, "Measurement errors induced by deformation of optical axes of achromatic waveplate retarders in RRFP Stokes polarimeters," Opt. Express 20(24), 026649 (2012).
- $^{\mathbf{45}}$ S. von Arnoldt, "Rotating quarter-wave plateplate Stokes polarimeter," Bachelor thesis (Universität Bonn, 2012).
- <sup>46</sup>B. Boulbry, B. L. Jeune, F. Pellen, J. Cariou, and J. Lotrian, "Identification of error parameters and calibration of a double-crystal birefringent wave plate with a broadband spectral light source," J. Phys. D: Appl. Phys. 35(20), 2508-2515 (2002).
- <sup>47</sup>B. Boulbry, B. Bousquet, B. L. Jeune, Y. Guern, and J. Lotrian, "Polarization errors associated with zero-order achromatic quarter-wave plates in the whole visible spectral range," Opt. Express 9(5), 225 (2001).
- <sup>48</sup>H. Hurwitz and R. C. Jones, "A new calculus for the treatment of optical SystemsII proof of three general equivalence theorems," J. Opt. Soc. Am. 31(7), 493 (1941).
- <sup>49</sup>E. M. Therézio, S. F. C. da Silva, G. G. Dalkiranis, P. Alliprandini Filho, G. C. Santos, F. Ely, I. H. Bechtold, and A. Marletta, "Light polarization states of a cholesteric liquid crystal probed with optical ellipsometry," Opt. Mater. 48, 7-11 (2015).
- <sup>50</sup>F. C. Basilio, P. T. Campana, E. M. Therézio, N. M. Barbosa Neto, F. Serein-Spirau, R. A. Silva, O. N. Oliveira, and A. Marletta, "Ellipsometric Raman spectroscopy," J. Phys. Chem. C 120(43), 25101-25109 (2016).

- <sup>51</sup>G. G. Dalkiranis, E. M. Therézio, G. Conte, H. Gallardo, I. H. Bechtold, and A. Marletta, "Emission ellipsometry as a tool for luminescent liquid crystal phase transition identification," Phys Rev E 98(2), 022702 (2018).
- <sup>52</sup>S. V. Ulrich, T. Sutch, G. Szulczewski, M. Schweizer, N. M. Barbosa Neto, and P. T. Araujo, "Broadband polarized emission from P(NDI2OD-T2) polymer," J. Phys.: Condens. Matter 30(26), 265101 (2018).
- $^{53}$ S. V. Ulrich, "Stokes spectroscopy: The development of a novel method to acquire and interpret polarized emission spectra-Applications to poly (3hexylthiophene and p(ndi2od-t2)," Ph.D. thesis, The University of Alabama,
- <sup>54</sup>L. F. R. B. Toledo, D. A. Turchetti, C. Zanlorenzi, A. P. Glislere, B. Nowacki, A. Marletta, E. L. Kowalski, and L. C. Akcelrud, "Circularly polarized light from a series of chiral fluorene copolymers," IEEE Photonics J. 11(1), 1-9 (2019).
- 55 L. F. R. B. Toledo, D. A. Turchetti, A. P. Glislere, B. Nowacki, F. C. Basílio, A. Marletta, E. L. Kowalski, and L. Akcelrud, "Correlation of electronic and vibrational properties with the chiro-optical activity of polyfluorene copolymers," Spectrochim. Acta, Part A 276, 121180 (2022).
- 56 F. E. Lucas, A. Marletta, R. S. Nobuyasu, J. V. G. de Araújo, G. A. de Souza, R. Lopes, O. N. Oliveira, and P. A. Filho, "Unraveling the morphology and macroscopic alignment of poly (9,9-di-n-octylfluorenyl-2,7-diyl) for enhanced polarized emission," ACS Appl. Polym. Mater. 2(12), 5406-5413 (2020).
- 57 E. M. Therézio, G. G. Dalkiranis, A. A. Vieira, H. Gallardo, I. H. Bechtold, P. T. Campana, and A. Marletta, Ellipsometry—Principles and Techniques for Materials Characterization (InTech, 2017).
- <sup>58</sup>G. G. Stokes, Mathematical and Physical Papers (Cambridge University Press, 2009), pp. 233-258.
- 59 J. D. Jackson, Classical Electrodynamics, 3rd ed. (John Wiley & Sons, Berkeley,
- $^{\bf 60}$  E. Hecht, Optics, 5th ed. (Pearson, 2017).
- $^{61}$ E. Hecht, "Note on an operational definition of the Stokes parameters," Am. J. Phys. 38, 1156-1158 (1970).
- $^{\bf 62} J.$  S. Tyo, D. L. Goldstein, D. B. Chenault, and J. A. Shaw, "Review of passive imaging polarimetry for remote sensing applications," Appl. Opt. 45(22), 5453
- $^{\bf 63}{\rm H.}$  Gu, S. Liu, X. Chen, and C. Zhang, "Calibration of misalignment errors in composite waveplates using Mueller matrix ellipsometry," Appl. Opt. 54(4), 684 (2015).
- <sup>64</sup>H. Gu, X. Chen, H. Jiang, C. Zhang, and S. Liu, "Optimal broadband Mueller matrix ellipsometer using multi-waveplates with flexibly oriented axes," J. Opt. 18(2), 025702 (2016).
- <sup>65</sup>H. Gu, X. Chen, H. Jiang, C. Zhang, W. Li, and S. Liu, "Accurate alignment of optical axes of a biplate using a spectroscopic Mueller matrix ellipsometer," Appl. Opt. 55(15), 3935 (2016).
- <sup>66</sup> H. Gu, X. Chen, Y. Shi, H. Jiang, C. Zhang, P. Gong, and S. Liu, "Comprehensive characterization of a general composite waveplate by spectroscopic Mueller matrix polarimetry," Opt. Express 26(19), 025408 (2018).
- <sup>67</sup>J. L. Vilas, L. M. Sanchez-Brea, and E. Bernabeu, "Optimal achromatic wave retarders using two birefringent wave plates," Appl. Opt. 52(9), 1892 (2013).
- <sup>68</sup> A.-B. Mahler, S. McClain, and R. Chipman, "Achromatic athermalized retarder fabrication," Appl. Opt. 50(5), 755 (2011).
- <sup>69</sup> A. Messaadi, M. . d.M. Sánchez-López, P. García-Martínez, A. Vargas, and I. Moreno, "Optical system for measuring the spectral retardance function in an extended range," J. Eur. Opt. Soc. 12(1), 21 (2016).
- $^{70}$ T. W. Cronin, "A different view: Sensory drive in the polarized-light realm," Curr. Zool. 64(4), 513-523 (2018).
- $^{71}\mathrm{G.}$  Garab and H. van Amerongen, "Linear dichroism and circular dichroism in photosynthesis research," Photosynth. Res. 101(2-3), 135-146 (2009).
- 72 K. A. Kistler, C. M. Pochas, H. Yamagata, S. Matsika, and F. C. Spano, "Absorption, circular dichroism, and photoluminescence in perylene diimide bichromophores: Polarization-dependent H- and J-aggregate behavior," J. Phys. Chem. B 116(1), 77-86 (2012).

- <sup>73</sup>S. C. J. Meskers, "Circular polarization of luminescence as a tool to study molecular dynamical processes," ChemPhotoChem 6(1), e202100154 (2022).
  <sup>74</sup>G. Pescitelli, L. Di Bari, and N. Berova, "Application of electronic circular"
- dichroism in the study of supramolecular systems," Chem. Soc. Rev. 43(15), 5211–5233 (2014).

  75 A. Rodger, Encyclopedia of Analytical Chemistry (John Wiley & Sons, Ltd,
- Chichester, UK, 2014), pp. 1-34.
- <sup>76</sup>H. Tanaka, Y. Inoue, and T. Mori, "Circularly polarized luminescence and circular dichroisms in small organic molecules: Correlation between excitation and emission dissymmetry factors," ChemPhotoChem 2(5), 386-402 (2018).

  77

  J. Kumar, T. Nakashima, H. Tsumatori, and T. Kawai, "Circularly polarized
- luminescence in chiral aggregates: Dependence of morphology on luminescence dissymmetry," J. Phys. Chem. Lett. 5(2), 316-321 (2014).